Journal of Electroanalytical Chemistry 1008 (2026) 119920

Contents lists available at ScienceDirect

Journal of Electroanalytical Chemistry

journal homepage: www.elsevier.com/locate/jelechem

Enhanced borohydride oxidation kinetics with Au@MOF-808 nanocomposite electrocatalysts with ultra-low Au loading

Ines Belhaj [a], J. Alexander Becker [a,b], Alexandre M. Viana [c], Filipe M.B. Gusmão [a], Miguel Chaves [c], Eulália Pereira [c], Biljana Šljukić [a], Salete S. Balula [c,d], Luís Cunha-Silva [c,e,**], Diogo M.F. Santos [a,*]

[a] Centre of Physics and Engineering of Advanced Materials, Laboratory of Physics for Materials and Emerging Technologies, Chemical Engineering Department, Instituto Superior Técnico, Universidade de Lisboa, 1049-001 Lisbon, Portugal
[b] Technical University Clausthal, 38678 Clausthal-Zellerfeld, Germany
[c] LAQV-REQUIMTE, Department of Chemistry and Biochemistry, Faculty of Sciences, University of Porto, 4169-007 Porto, Portugal
[d] LAQV / REQUIMTE & Department of Chemistry, Nova School of Science and Technology, Nova University of Lisbon, 2829-516 Monte da Caparica, Portugal
[e] Laboratório Nacional de Energia e Geologia (LNEG) I.P., Estrada do Paço do Lumiar 22, 1649-038 Lisboa, Portugal

ARTICLE INFO

Keywords:
Gold
Metal-organic framework
borohydride oxidation reaction
Direct borohydride fuel cell

ABSTRACT

The highly stable metal-organic framework (MOF) composed of $[Zr_6O_4(\mu_3\text{-}OH)_4(OH)_6(H_2O)_6(BTC)_2]\cdot nH_2O$ units (MOF-808) was modified by incorporating gold (Au) nanoparticles and functional groups to enhance electrocatalytic activity for the borohydride oxidation reaction (BOR). Three composite materials (Au@MOF-808, Au@MOF-808-NH_2, and Au@MOF-808-SH) were prepared by the incorporation of Au in structurally related MOFs, MOF-808, MOF-808-NH_2, and MOF-808-SH, respectively. These composite materials were evaluated as anodic electrocatalysts for BOR in alkaline media using cyclic voltammetry and chronoamperometry. Among the prepared materials, Au@MOF-808-NH_2 exhibited the highest BOR activity, with an apparent activation energy of 15.3 kJ mol^{-1}, a reaction order of 0.6, an anodic charge transfer coefficient of 0.63, and a number of exchanged electrons of 4.4. The latter was significantly below the theoretical eight-electron value, indicating the presence of alternative reaction pathways. Notably, this material achieved a high mass-specific BOR peak current of 4.23 A μg_{Au}^{-1}, demonstrating outstanding electrocatalytic efficiency despite the ultralow noble metal loading. These results underscore the potential of Au@MOF-808-NH_2 as a cost-effective and scalable anodic electrocatalyst for high-performance direct borohydride fuel cells.

1. Introduction

Energy production and consumption are the largest contributors to global greenhouse gas emissions [1]. Fuel cells powered by hydrogen offer a clean energy source, but face challenges related to hydrogen cost and infrastructure. Direct liquid fuel cells (DLFCs) offer a potential solution by using liquid fuels such as methanol or ethanol, which are easier to store and transport. Among DLFCs, direct borohydride fuel cells (DBFCs) stand out for their high energy density, low operating temperatures, and zero carbon emissions, making them particularly suitable for applications such as space and underwater vehicles [2]. Based on hypothetical models, the specific power output of DBFCs is assumed to be 600–1000 Wh kg^{-1}, which is five to six times that of state-of-the-art lithium-ion batteries [3]. The fuel used in DBFCs is a highly alkaline sodium borohydride ($NaBH_4$) medium. The borohydride oxidation reaction (BOR) at the DBFC anode is given by Eq. 1,

$$\text{Anode: } NaBH_4 + 8OH^- \rightarrow NaBO_2 + 6H_2O + 8e^- \qquad E^0 = -1.24\,\text{V vs. SHE} \tag{1}$$

where E^0 represents the standard electrode potential of BOR against the standard hydrogen electrode (SHE). As there is always some production of hydrogen gas due to the unwanted partial hydrolysis of the borohydride ion (BH_4^-) (Eq. 2), the possibility of this reaction occurring as a parasitic reaction cannot be ignored. Thus, considering the parasitic BH_4^- hydrolysis, the borohydride oxidation process can be written as Eq. 3,

* Corresponding author.
** Corresponding author at: Laboratório Nacional de Energia e Geologia (LNEG) I.P., Estrada do Paço do Lumiar 22, 1649-038 Lisboa, Portugal.
E-mail addresses: luis.csilva@lneg.pt (L. Cunha-Silva), diogosantos@tecnico.ulisboa.pt (D.M.F. Santos).

https://doi.org/10.1016/j.jelechem.2026.119920
Received 4 November 2025; Received in revised form 30 January 2026; Accepted 2 February 2026
Available online 5 February 2026

$$BH_4^- + H_2O \rightarrow H_2 + BH_3OH^- \quad (2)$$

$$BH_4^- + xH_2O \rightarrow B(OH)_4^- + (x-4)H_2O + (4-x/2)H_2 + xe^- \quad (3)$$

where "x" is the coulombic number. The x value can be obtained experimentally using standard electrochemical methods, such as cyclic voltammetry and rotating disc electrode measurements, or by measuring the volume of hydrogen gas produced. The x value ranges from 0 to 8, typically 4, when using platinum (Pt)-based electrodes.

On the cathode side of the DBFC, oxygen (O_2) is adsorbed onto the electrode and reduced according to Eq. 4. By combining Eqs. 1 and 4, the net cell reaction of a typical DBFC is given by Eq. 5, with a theoretical cell voltage of 1.64 V at 25 °C [2].

$$\text{Cathode}: O_2 + 2H_2O + 4e^- \rightarrow 4OH^- \qquad E^0 = 0.40 \text{ V vs.SHE} \quad (4)$$

$$\text{Overall}: BH_4^- + 2O_2 \rightarrow BO_2^- + 2H_2O \qquad E_{cell}{}^0 = 1.64 \text{ V} \quad (5)$$

The most critical design factors for DBFC are the selection of the membrane, electrolyte, and electrocatalysts. This means that identifying suitable and promising electrocatalysts for DBFCs is crucial to the development of these power sources. Thus, choosing an electrocatalyst with high electrocatalytic activity toward BOR, inactivity toward the competing hydrolysis reaction, stability, durability, and a low price is essential [5–7]. The electrocatalysts utilised in DBFCs can be generally classified into three groups: noble metals (e.g., Pt, palladium (Pd), gold (Au)), transition metals (e.g., iron (Fe), cobalt (Co), nickel (Ni)), and their corresponding alloys [5].

Au electrocatalysts supported on traditional carbonaceous materials have shown superior activity, chemical stability, and selectivity for BOR compared to transition metals, thereby reducing side reactions such as parasitic BH_4^- hydrolysis [7,8]. Modifications of Au nanoparticles (NPs), such as oleylamine treatment, have further enhanced electrocatalytic performance by stabilising partially oxidised Au surfaces that are favourable for BH_4^- adsorption [7].

Xue et al. developed a multisite CoFe–Au electrocatalyst that achieved good BOR selectivity and high power density via a tandem electrocatalytic mechanism involving CoFe layered double hydroxides and Au NPs [9]. Bimetallic AuNi and AuCo electrocatalysts supported on carbon nanotubes have also demonstrated enhanced BOR activity and durability due to synergistic effects between metals and the conductive carbon supports [10,11]. Yi et al. tested carbon-supported Au—Fe bimetallic nanocatalysts (Au-Fe/C) as anode electrocatalysts for DBFCs. Their results showed that Au-Fe/C electrocatalysts exhibited higher electrocatalytic activity for the direct electrooxidation of BH_4^-, particularly the $Au_{50}Fe_{50}$/C electrocatalyst. A DBFC with $Au_{50}Fe_{50}$/C anode and Au/C cathode gave a peak power density of 34.9 mW cm^{-2} at 25 °C [12]. Duan et al. studied carbon-supported Co—Au bimetallic NPs with different Co/Au atomic ratios as anode electrocatalysts for BOR, prepared via a two-step reduction in a reverse microemulsion system. Co_4–Au_1/C presented the highest electrocatalytic activity for BOR, and the DBFC assembled with these anodic electrocatalysts showed a peak power density of 102 mW cm^{-2} [13].

MOFs are a class of crystalline, porous materials assembled from metal-based nodes and single or multiple organic linkers, forming large, highly open one-, two-, or three-dimensional networks with photo- and electroactive ligands and metal ions. They have been demonstrated to be efficient electron acceptors with suitable catalytic sites that boost various energy-related chemical reactions [4,14–20].

Studies on the use of MOF-based electrocatalysts for BOR are limited, but demonstrate significant potential. For instance, Backović et al. developed a new material based on ruthenium (Ru) NPs stabilised by Fe-BTC (Basolite F-300) MOF (Ru@Fe-BTC), which proved to be a promising electrocatalyst for BOR. Their lab-scale direct borohydride/peroxide fuel cell, assembled using Ru@Fe-BTC as an anodic electrocatalyst, delivered a high peak power density of 169 mW cm^{-2} at 65 °C [20]. Therefore, despite the limited literature, MOF-based supports, such as MOF-808, offer notable advantages over traditional carbon supports. As reported by Sun et al. [21], MOFs enable precise control over metal-support interactions, local electronic environments, and the spatial distribution of active sites, which is particularly beneficial for noble metals like Au, where high dispersion and stability at ultralow loadings are crucial. In the herein-reported electrocatalyst, functionalised MOF-808 enhances Au utilisation and activity at low potentials, likely due to improved accessibility of BH_4^- ions, reduced NP aggregation, and electron-donating effects from amine or thiol linkers.

Furthermore, MOF-808, a zirconium-based framework made from Zr_6 nodes and trimesic acid linkers, exhibits exceptional alkaline stability, large mesoporous structure, and high surface area, providing ample space for the uniform dispersion of AuNPs. Unlike carbon supports, its chemically tailorable architecture allows for post-synthetic functionalisation (e.g., –NH_2, –SH), which can tune the electronic environment and enhance metal–support interactions, thereby stabilising electrocatalytically active surface states.

Thus, while most BOR studies highlight advances in Au-based electrocatalysts (and their alloys) anchored on typical support materials, such as carbon or carbon nanotubes, the use of MOFs as supports for BOR electrocatalysts remains comparatively unexplored. Conventional supports can provide good conductivity, but lack the structural tunability and high surface area that MOFs offer. In particular, MOF-808 provides a porous, chemically stable, and highly tailorable platform for uniformly dispersing Au NPs, enabling ultralow noble metal loadings while maintaining, or even enhancing, electrocatalytic activity and durability. Thus, this ultralow Au loading can enable lower-cost BOR electrocatalysts while maintaining the required electrocatalytic activity.

Building on the performance benchmarks established by conventional Au-based electrocatalysts, this work investigates Au/MOF-808 nanocomposites as an alternative electrocatalyst design for the BOR. By incorporating Au NPs into the MOF framework, the aim is to leverage MOF-specific properties to enhance reaction kinetics, selectivity, and long-term stability beyond what is achievable with traditional supports. The nanocomposites were evaluated for their electrocatalytic performance using voltammetric and chronoamperometric techniques, with a focus on both activity and operational stability.

2. Experimental

2.1. Materials and chemicals

The following chemicals were used in the synthesis of the materials: Zirconium(IV) chloride ($ZrCl_4$, 99.5%), gold(III) chloride solution ($HAuCl_4$, 99.99%, in 30 wt% HCl), sodium borohydride ($NaBH_4$, 99%), trimesic acid ($C_9H_6O_6$, 95%), and cysteamine (C_2H_7NS, 99%) were supplied by Sigma-Aldrich. 4-mercaptobenzoic acid ($C_7H_6O_2S$, 99%) was provided by Acros. Alfa Aesar supplied 4-aminobenzoic acid ($C_7H_7O_2N$, 99%). Sodium hydroxide (NaOH, 98%) was supplied by Fluka. Acetic acid (CH_3CO_2H, 100%) was supplied by Ensure. Fisher supplied dimethylformamide (DMF, 99.99%). For electrochemical studies, Nafion (5 wt%) was purchased from Sigma-Aldrich, ethanol (C_2H_5OH, 96 vol%) from FÁBRICA DO ÁLCOOL, $NaBH_4$ (95–98 wt%, synthesis grade) from Scharlau, and NaOH (99–99.5 wt%, pellets, analytical reagent grade) from Fisher Scientific. All solutions were prepared using Millipore water (Milli-Q®, Merck, USA).

2.2. Synthesis of the materials

2.2.1. MOF-808

The MOF-808 material was prepared according to procedures previously described [22]. A mixture of $ZrCl_4$ (1.5 mmol) and trimesic acid (0.5 mmol) in DMF (15 mL) and acetic acid (9 mL) was sonicated for 30 min. The mixture was then transferred to an autoclave. The reaction mixture was left in an oven at 130 °C for 48 h. The solid material obtained was isolated by centrifugation, washed several times with EtOH,

and dried overnight at 60 °C and 120 mbar.

2.2.2. MOF-808-NH_2 and MOF-808-SH

The two MOF-based materials, MOF-808-NH_2 and MOF-808-SH, were prepared by post-synthetic modification of previously obtained MOF-808. For each material, pristine MOF-808 (100 mg) was dispersed in a DMF solution (20 mL) containing an excess of either 2-aminobenzoic acid (for MOF-808-NH_2) or 4-mercaptobenzoic acid (for MOF-808-SH). The respective mixtures were stirred at 65 °C for 24 h, and each resulting material was then centrifuged and suspended in fresh DMF (10 mL) for 48 h at room temperature. The materials were recovered by centrifugation, washed several times with anhydrous acetone, and dried overnight at 60 °C and 120 mbar.

2.2.3. Au@MOF-808-based nanocomposites

To prepare the Au@MOF-808-based nanocomposite materials, 100 mg of each initial MOF material (MOF-808, MOF-808-NH_2, or MOF-808-SH) was dispersed in 10 mL of an aqueous $HAuCl_4$ solution (51 μM). The respective mixtures were sonicated for 15 min and then left under magnetic stirring for 5 days. Each obtained solid was recovered by centrifugation, redispersed in 5 mL of deionised water, and stirred at a low temperature (in an ice bath). Subsequently, 5 mL of an alkaline $NaBH_4$ solution (0.044 M) was added to each mixture, which was stirred for 1 h. The isolated materials (Au@MOF-808, Au@MOF-808-NH_2, and Au@MOF-808-SH) were recovered by centrifugation, washed several times with deionised water, and dried overnight at 75 °C under vacuum.

2.3. Characterisation of the materials

Fourier-transform infrared (FT-IR) spectra were acquired on the attenuated total reflectance (ATR) operation mode of a PerkinElmer FT-IR System Spectrum BX spectrometer. All spectra are shown in arbitrary units of transmittance. Powder X-ray diffraction (PXRD) patterns were obtained at room temperature on a Rigaku Geigerflex diffractometer operating with CuKα radiation source ($\lambda_1 = 1.540598$ Å; $\lambda_2 = 1.544426$ Å; $\lambda_1/\lambda_2 = 0.500$) and in a Bragg-Brentano $\theta/2\theta$ configuration (45 kV, 40 mA). Intensity data were collected using a step-counting method (step size 0.026°) in continuous mode, within the $3° \leq 2\theta \leq 70°$ range. All representations are shown in arbitrary units of intensity. Scanning electron microscopy (SEM) and energy-dispersive X-ray spectroscopy (EDS) analysis were performed using a FEI Quanta 400 FEG ESEM high-resolution scanning electron microscope equipped with an EDAX Genesis X4M spectrometer, operating at 15 kV. Samples were coated with a thin Au/Pd film by sputtering using the SPI Module Sputter Coater. Inductively coupled plasma optical emission spectroscopy (ICP-OES) was used to quantify Au concentrations in various samples using a PerkinElmer Optima 4300 DV. X-ray photoelectron spectroscopy (XPS) spectra were collected using an ESCALAB 250 iXL instrument (VG Scientific) with an aluminium anode operating at 15 kV (300 W) at Universidade de Vigo, CACTI.

2.4. Electrochemical measurements

The electrochemical measurements to examine BOR kinetics were performed in a three-electrode setup using an 80 mL glass cell, a Squidstat potentiostat, and the associated software from Admiral Instruments. Each MOF-based material was tested using a glassy carbon working electrode, while a Pt mesh served as the counter electrode. Electrocatalyst inks were prepared by adding 100 μL of Nafion as the binder, 5 mg of MOF, 400 μL of ethanol, and 600 μL of H_2O. Then, 15 μL of the electrocatalyst ink was pipetted onto an ElectraSyn 2.0 glassy carbon electrode (0040002842, IKA, Wilmington, NC, USA) with an active geometric surface area of 0.6 cm^2. All potential measurements were conducted versus a saturated calomel electrode (SCE, HANNA Instruments HI5412), and the values were converted to the reversible hydrogen electrode (RHE) scale for further data analysis. Accordingly, all potentials presented are referred to the RHE reference. The electrochemical characterisation was carried out in an alkaline solution of 0.03 M $NaBH_4$ (Scharlau, powder, synthesis grade) in 2 M NaOH (Fisher Scientific, pellets, analytical reagent grade), serving as the supporting electrolyte and providing a strong alkalinity to the solution (pH = 14.3). Initial cyclic voltammograms (CVs) were performed at 50 mV s^{-1} and 25 °C in a 2 M NaOH solution, followed by the addition of 0.03 M $NaBH_4$. The dependence of current density on scan rate was examined by recording linear scan voltammograms (LSVs) in $NaBH_4$ solution at 25 °C, increasing the scan rate from 5 to 1000 mV s^{-1}. Based on these initial screenings, two materials, Au@MOF808-NH_2 and Au@MOF808-SH, were selected for further electrochemical studies based on their promising activity toward BOR. These studies focused on the correlation between current density and temperature in the 25–65 °C range, as well as on the effect of $NaBH_4$ concentration, ranging from 0.01 to 0.12 M, on BOR kinetics. Chronoamperometric (CA) measurements were carried out in a 2 M NaOH +0.03 M $NaBH_4$ solution holding the working electrode potential at 0.9 V for 7200 s.

3. Results and discussion

3.1. Characterisation of the MOF-based materials

MOF-808 is a well-known and highly stable MOF based on $[Zr_6O_4(\mu_3\text{-}OH)_4(OH)_6(H_2O)_6(BTC)_2]\cdot nH_2O$ building units to form a porous framework containing accessible acidic cavities with an internal diameter of ca. 18 Å [14]. **Fig. S1** in the Supplementary Information document (SI) shows the PXRD patterns acquired for the obtained MOF-808-based samples. The diffraction profile observed for MOF-808 matches the characteristic and previously reported pattern for this crystalline framework [15]. All materials exhibit the same expected diffraction profile, with slightly variable degrees of crystallinity, indicating the preservation of the framework after post-synthetic modification and Au NP incorporation. The characteristic diffraction reflections of Au NPs are also clearly observable for both Au@MOF808-NH_2 and Au@MOF808-SH, with the latter exhibiting the most reduced degree of crystallinity after incorporating Au NPs.

Fig. S2 in the SI shows the FT-IR spectra recorded for the various MOF-808-based samples. All spectra show the main characteristic bands expected from the MOF molecular structure: a weak absorption band at 1660 cm^{-1} related to the bond vibrations of acetate groups coordinated with the oxo-clusters; medium and strong intensity bands attributable to vibrational modes of the carboxylate groups around 1580 and 1380 nm; a medium intensity band at 1440 cm^{-1} ascribed to aromatic (C=C) bond vibrations; a group of bands registered between 775 and 600 cm^{-1} associated with vibrational modes of Zr − (μ_3-O) framework bonds; a weak band around 450 nm related with Zr − (OC) bonds [14]. Additionally, a pair of weak bands can be observed in the spectra of the post-synthetically modified samples in the interval between 3050 and 2850 cm^{-1}, which can be attributed to vibrations of (N − H) or (S − H) bonds, respectively.

SEM micrographs obtained for the various Au@MOF-808 nanocomposite materials are revealed in Fig. 1. Au@MOF-808 displays well-distributed Au NPs throughout the sample, with an estimated diameter of 13 to 60 nm (Fig. 1a). With a larger size distribution, Au@MOF-808-NH_2 shows Au NPs between 60 and 270 nm (Fig. 1b). The largest Au NPs observed for both groups of materials are those of Au@MOF-808-SH, which range in diameter from 200 to 600 nm (Fig. 1c). Acquired EDS confirms the presence of every expected element for each sample, particularly Au and Zr (Fig. 1).

XPS is important for determining the oxidation states of different species. However, this is a surface analysis technique that examines the top 0–10 nm of the sample. A high-resolution XPS spectrum of the Au 4f core level collected for Au@MOF-808 composites prepared in relatively concentrated suspensions shows bands for Au $4f_{7/2}$ and Au $4f_{5/2}$ that can result from contributions of two pairs of peaks arising from Au^0, Au^{1+}, or

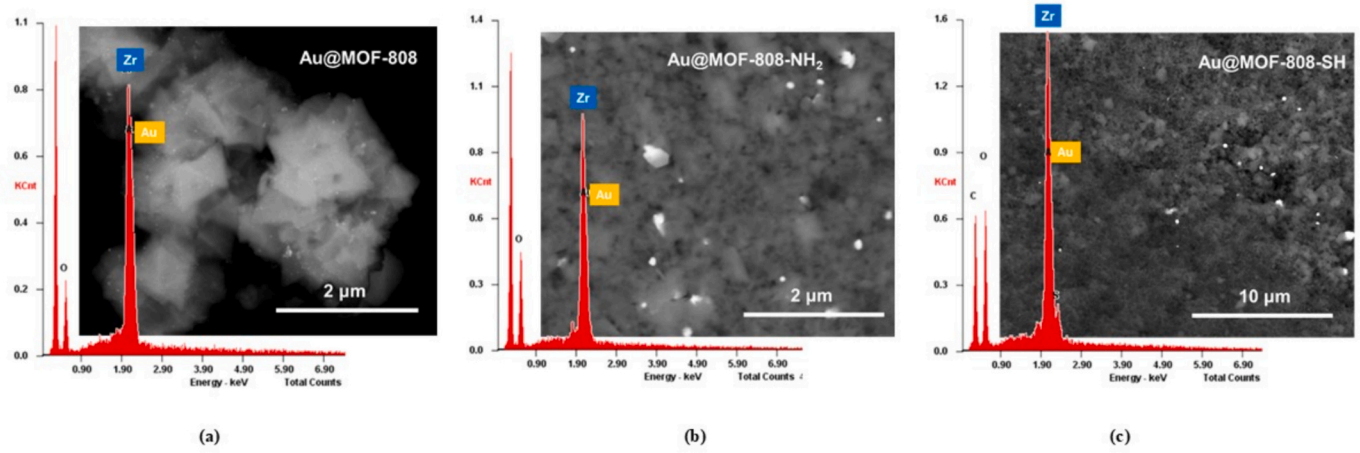

Fig. 1. SEM micrographs and respective EDS spectra obtained for (a) Au@MOF-808, (b) Au@MOF-808-NH_2, and (c) Au@MOF-808-SH.

even Au^{3+} states presented on the surface of composites. For the Au@MOF-808 composite, the peaks at 83.9 and 87.6 eV correspond to Au^0 $4f_{7/2}$ and Au^0 $4f_{5/2}$, respectively. Paired with peaks at 85.1 and 88.8 correspond to Au^{1+} level, and 86.2 and 89.9 correspond to Au^{3+}. The estimated composition of Au^0, Au^{1+} and Au^{3+} is 8.6%, 17.5% and 73.9%. The same study was performed for the functionalized Au@MOF-808 composites. Results are presented in Table 1 and **Fig. S3** in the SI. It is possible to observe that the non-functionalized composite presents reduced Au^0 on the surface and also a considerable amount of Au that did not reduce Au^{3+}. The functionalized composites showed a higher amount of reduced Au on their surfaces. In general, a range of oxidation states of Au is observed across all MOF-808 samples. Furthermore, the identified Au 4f peak positions are slightly shifted to higher energies in relation to expected characteristic binding energies when functional -NH_2 and -SH groups were introduced. This may indicate a significant interaction of Au with its environment [23].

3.2. *Electrocatalytic response of Au@MOF-808-NH_2 toward BH_4^- oxidation*

The electrocatalytic activity of the MOF-based working electrodes toward the oxidation of BH_4^- was initially examined by recording CVs in $NaBH_4$ solution at 25 °C. Fig. 2a shows the comparative CVs of the Au@MOF-808-NH_2 electrode in 2 M NaOH without (shown in the inset) and with BH_4^- in the solution. Currents are negligible in 2 M NaOH solution and significantly increase when 0.03 M $NaBH_4$ is added, indicating that the observed redox processes result from the electrooxidation of BH_4^-.

The BOR onset potential, E_{onset}, at Au@MOF-808-NH_2 was observed to be 0.41 V. The voltammogram in the BH_4^- solution is rather complex, consisting of two oxidation peaks on the forward (anodic) scan and two oxidation peaks on the backscan. Au@MOF-808-NH_2 shows a first oxidation peak occurring at potential E_{p1} of 0.93 V with current density j_{p1} of 25.6 mA cm^{-2}, followed by a smaller peak at E_{p2} of 1.23 V with j_{p2} of 16.1 mA cm^{-2}. The backscan oxidation peaks appear at E_{p3} of 1.25 V with j_{p3} of 28.5 mA cm^{-2} and E_{p4} of 0.93 V with j_{p4} of 14.6 mA cm^{-2}. The oxidation peaks observed on the cathodic scan result from the oxidation of adsorbed intermediates formed during the anodic scan, giving the CV a surprisingly symmetrical shape. Moreover, the decrease in current observed at potentials above 1.3 V vs. RHE is primarily due to the formation of surface gold oxides (Au–OH/Au–O). These gold oxides are catalytically inactive toward the oxidation of BH_4^-, thereby suppressing further oxidative processes. When the potential is then scanned in the cathodic direction, the electrochemical reduction of these surface oxides occurs, restoring the active Au sites. This surface reactivation enables the immediate oxidation of reaction intermediates adsorbed or accumulated on the electrode surface during the anodic scan, resulting in a sharp oxidation peak (p_3, Fig. 2a).

Au@MOF-808-NH_2 shows notably higher peak current densities than the other three tested materials (Fig. 2b), suggesting significantly higher activity toward BOR. For comparison purposes, the CVs of the four materials recorded in a 2 M NaOH solution in the absence of $NaBH_4$ are also presented in **Fig. S4**. Although Au@MOF-808-NH_2 exhibits negligible currents, as shown in the inset of Fig. 2a, the other three materials reveal significant cathodic instability in alkaline media, thus affecting catalytic activity. Based on Fig. 2b, the BOR peak 1 current densities decreased in the following order: Au@MOF-808-NH_2 @25.6 mA cm^{-2} > Au@MOF-808-SH @3.55 mA cm^{-2} > Au@MOF-808 @0.94 mA cm^{-2} > MOF-808 @0.04 mA cm^{-2}. This trend is particularly noteworthy when considering the Au loading (Table 2).

To clarify the data in Table 2, to convert from molality (b_{Au}, $\mu mol_{Au} g_{MOF}^{-1}$) to concentration ($c_{Au}$, mg_{Au} g_{MOF}^{-1}), molality is multiplied by 0.197 mg μmol^{-1}, based on the molar mass of Au. To calculate the mass of Au on the electrode (m_{Au}), the concentration (c_{Au}, mg_{Au} g_{MOF}^{-1}) is multiplied by the mass of MOF applied to the working electrode, which is determined to be 0.045 mg.

Au@MOF-808-NH_2 and Au@MOF-808-SH show the highest mass-specific peak current of 4.23 A μg_{Au}^{-1} and 0.51 A μg_{Au}^{-1}, respectively. These two materials have a minimal Au loading, approximately two orders of magnitude lower than that of Au@MOF-808. The Au@MOF-808-NH_2 exceptional performance, highlighted by its high mass-specific current, demonstrates its ability to maximise electrocatalytic efficiency while minimising Au loading. This indicates that the observed BOR electrocatalytic activity is not solely correlated to the Au loading but rather related to the functionalisation of the used ligands with NH_2 and SH groups. Notably, the NH_2 functional group significantly enhances the electrocatalytic activity of the MOF nanocomposite for BOR. Nonetheless, the presence of Au NPs is essential for BOR electrocatalysis, whether alone or in synergy with the introduced SH and NH_2 functional groups. Next, LSVs were recorded at scan rates ranging from 5 to 200

Table 1
Identification and relative surface distribution of gold species in Au@MOF-808 composites.

Sample	Au $4f_{7/2}$ (eV)	Au $4f_{5/2}$ (eV)	Surface au species
Au@MOF-808	83.9	87.6	Au^0–8.6%
	85.1	88.8	Au^{1+} – 17.5%
	86.2	89.9	Au^{3+} – 73.9%
Au@MOF-808-NH_2	84.1	87.6	Au^{1+} – 79.2%
	85.5	89.1	Au^{3+} – 20.8%
Au@MOF-808-SH	85.5	89.3	Au^{1+} – 70%
	86.8	90.7	Au^{3+} – 30%

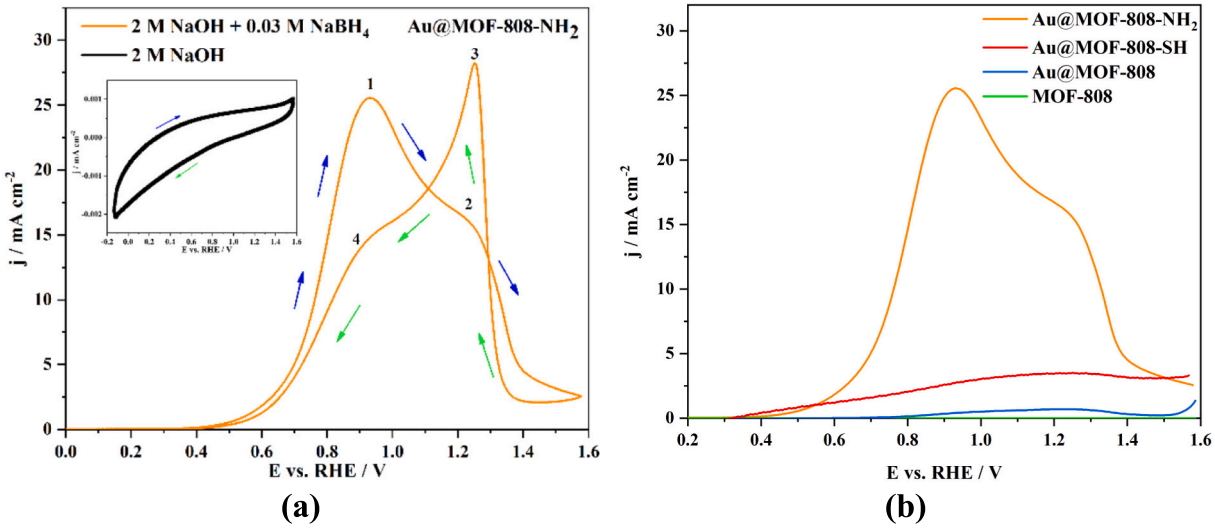

Fig. 2. (a) CVs Au@MOF-808-NH_2 in 2 M NaOH with and without (inset) 0.03 M $NaBH_4$ and (b) LSVs of the four materials in 0.03 M $NaBH_4$ in 2 M NaOH at 50 mV s^{-1}.

Table 2
Molality, concentration, mass loading of Au, peak current density at 50 mV s^{-1}, and corresponding mass-specific peak current of the studied Au-containing MOF-based electrocatalysts.

	Au@MOF-808	Au@MOF-808-NH_2	Au@MOF-808-SH
b_{Au} ($\mu mol_{Au}\ g_{MOF}^{-1}$)	32.5	0.27	0.31
c_{Au} ($mg_{Au}\ g_{MOF}^{-1}$)	6.40	0.05	0.06
m_{Au} (μg_{Au})	0.72	0.006	0.007
j_p (mA cm^{-2})	0.04	25.6	3.55
i_p (A μg_{Au}^{-1})	0.054	4.23	0.51

mV s^{-1}, as shown in Fig. 3.

The LSVs of Au@MOF-808-NH_2 exhibit notably high currents that increase gradually with the scan rate (Fig. 3c). Furthermore, peak potentials shift to more positive values with increasing scan rate, a feature typical of highly irreversible processes, further demonstrating the sluggish BOR kinetics at the Au@MOF-808-NH_2 electrode (Fig. 3c).

On the other hand, for Au@MOF-808, the recorded currents are significantly lower, and the peak potentials exhibit the opposite behaviour, shifting to more negative potential values with increasing scan rate (Fig. 3a). For Au@MOF-808-SH, the LSVs show a gradual increase in current density with increasing scan rate but lack well-defined oxidation peaks (Fig. 3b), with currents approximately one order of magnitude lower than those of Au@MOF-808-NH_2. This behaviour could be attributed to weaker adsorption or less efficient activation of BH_4^- at the SH-functionalised surface. It may indicate that the total number of active sites or the turnover frequency (or a combination of both) is limited. The -SH groups have a very strong affinity for Au, possibly resulting in partial "poisoning" or blocking of the Au surface, leading to low currents and no well-defined peaks, despite the early onset. The steady increase in current with increasing scan rate indicates that the material retains electrocatalytic activity, though with less favourable kinetics than its NH_2-functionalised counterpart. Furthermore, the current decrease in Au@MOF-808-SH at potentials >1.3 V vs. RHE is less pronounced than for the other two catalysts, which may also be related to the possible poisoning of Au sites by the SH species.

The values of the anodic charge transfer coefficient, α, were then determined using the equation that described the peak potential dependence on the logarithm of polarisation rate, E_p vs. ln ν, for irreversible processes [24] (Fig. 4a). Assuming the value for the number of electrons involved in the rate-determining step, n_a, to be 1, the α for BOR at the Au@MOF-808-NH_2 electrode was calculated to be 0.63.

Typically, a linear increase of peak current density, j_p, with the square root of the scan rate, $\nu^{1/2}$, is evidence that a process involving diffusion of species from the solution to the electrode surface (as opposed to adsorbed species in the case of a linear j_p-ν relation) is taking place at the electrode's surface. However, in the case of BH_4^- oxidation on Au@MOF-808-NH_2, this does not exclude simultaneous involvement of surface processes that may contribute to a mixed control mechanism. It is known that BOR is a multistep reaction involving (i) diffusion of BH_4^- from the bulk electrolyte to the electrode surface, (ii) adsorption and decomposition of BH_4^- into surface-bound intermediates, and (iii) electron-transfer steps associated with their oxidation. Herein, the linear j_p–$\nu^{1/2}$ relationship indicates that the mass transport of BH_4^- to the electrode surface is limiting the peak current. At the same time, the observed peak potential shift toward more positive values with increasing scan rate, along with quasi-symmetrical CV profiles, reflects the irreversible nature of the electron-transfer steps and the oxidation of adsorbed intermediates formed during the anodic scan. Thus, the BOR on Au@MOF-808-NH_2 is best described as a mixed-controlled process, in which diffusion and kinetic processes (surface processes, electron transfer) have comparable rates, and therefore both define the overall current.

The total number of exchanged electrons, n, could be determined from the slope of the j_p vs. $\nu^{1/2}$ plots (Fig. 4b) using the modified Randles-Sevcik equation for irreversible processes, considering a BH_4^- diffusion coefficient, D_{BH4}, of 1.21×10^{-5} $cm^2\ s^{-1}$ [25]. The obtained n value for Au@MOF-808-NH_2 was 4.4, lower than the expected theoretical maximum of 8 e^- per BH_4^- ion. This lower number of exchanged electrons indicates that the electrooxidation of BH_4^- at the MOF-based materials is not direct, or there is the occurrence of competing BH_4^- hydrolysis (Eq. 2). As stated earlier, two possible mechanisms for BH_4^- oxidation are the direct mechanism, involving 8 transferred electrons (Eq. 1), and the indirect mechanism, which typically involves 4 transferred electrons (Eq. 3). In the present case, the latter seems to be the followed mechanism.

The BOR kinetics of the two most responsive materials in the voltammetric analysis, Au@MOF-808-NH_2 and Au@MOF-808-SH, were further investigated by assessing the temperature dependence of the reaction rate. The increase in cell temperature is expected to increase current density by enhancing diffusion and, consequently, fuel mass transfer [26], which is related to a decrease in electrolyte viscosity [27]. Increasing the temperature also increases the BOR rate constant, thereby enhancing the charge-transfer process. It is to be noted, however, that for a practical DBFC application, the correlation between temperature

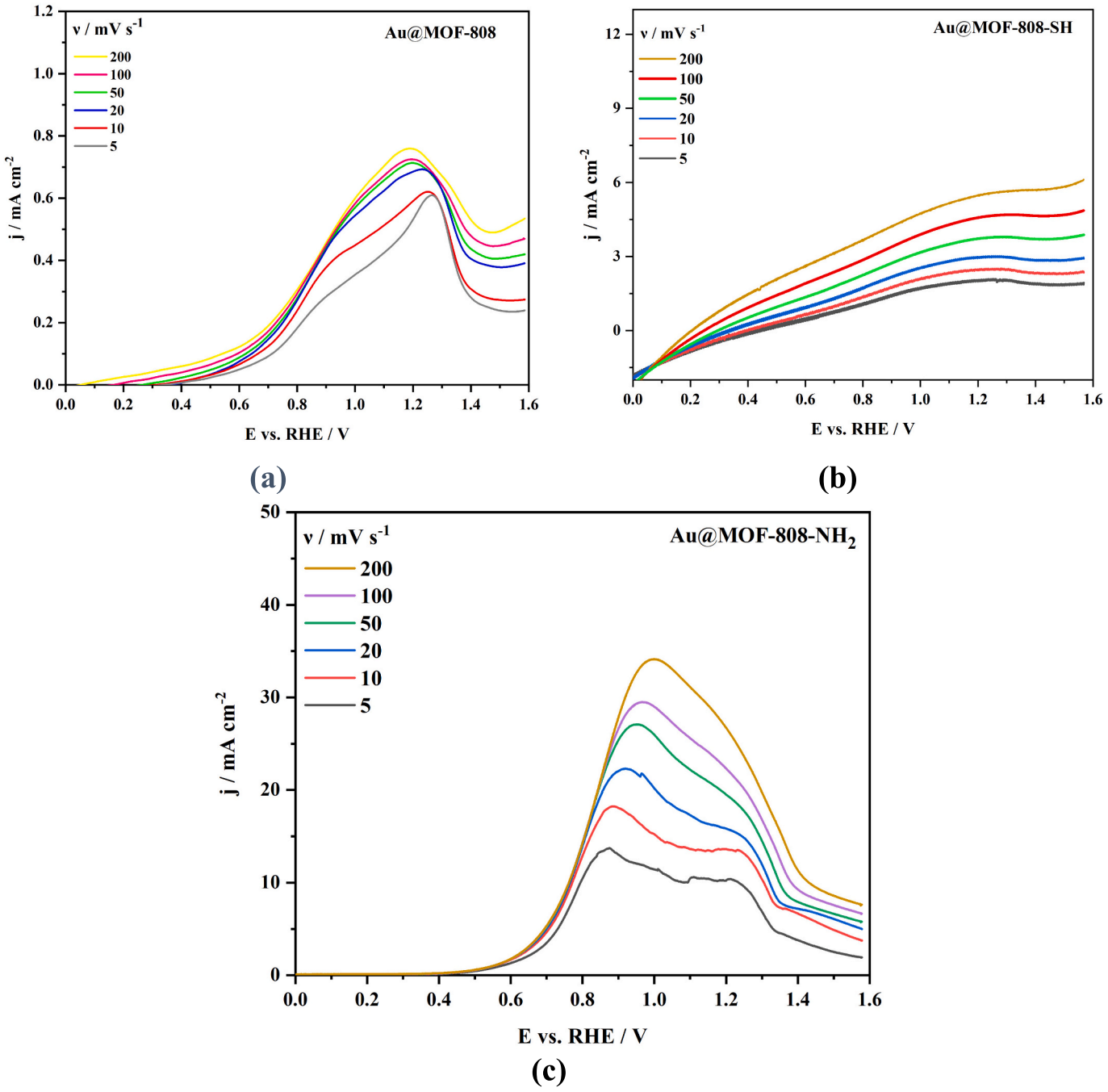

Fig. 3. LSVs of (a) Au@MOF-808, (b) Au@MOF-808-SH, and (c) Au@MOF-808-NH_2 in 0.03 M $NaBH_4$ in 2 M NaOH at 25 °C at different scan rates.

increase and current increase only applies until the upper threshold of temperature tolerance of the DBFC's membrane, as cell resistance increases due to partial drying of the membrane. In addition to membrane drying, the competing undesired hydrolysis reaction is favoured at high temperatures. This leads to a decrease in current density, as hydrolysis creates gas bubbles that attach to the electrode surface, thereby decreasing the effective surface area [26]. The temperature dependence was determined by recording LSVs in 0.03 M $NaBH_4$ at temperatures ranging from 25 to 65 °C (Fig. 5a). As Au@MOF-808-SH showed no increase in peak current density with increasing temperature, it was not possible to investigate the temperature dependence of BOR kinetics at this material. For Au@MOF-808-NH_2, higher operating temperatures increased current densities and shifted the oxidation peaks to more positive potentials. The increase in current density with operating temperature allows determination of the corresponding apparent activation energy, E_a^{app}, for BOR. Thus, by plotting the natural logarithm of the current densities recorded at 0.9 V as a function of the reciprocal temperature, it was possible to determine E_a^{app} by applying the Arrhenius equation and the slopes of the Arrhenius plots (Fig. 5b) [26]. The E_a^{app} for BOR at Au@MOF-808-NH_2 was found to be 15.3 kJ mol^{-1}, lower than the 17 kJ mol^{-1} reported for BOR catalysed by Ru NPs stabilised within a MOF [20]. This lower E_a^{app} value highlights the enhanced electrocatalytic efficiency of Au@MOF-808-NH_2. E_a^{app} reflects the energy barrier of both interfacial charge-transfer processes and BH_4^- diffusion, as commonly reported for multistep electrocatalytic reactions [28,29].

Although high $NaBH_4$ concentrations are desirable to increase the energy density of DBFCs, it must be considered that increasing $NaBH_4$ concentration also increases the rate of the detrimental $NaBH_4$

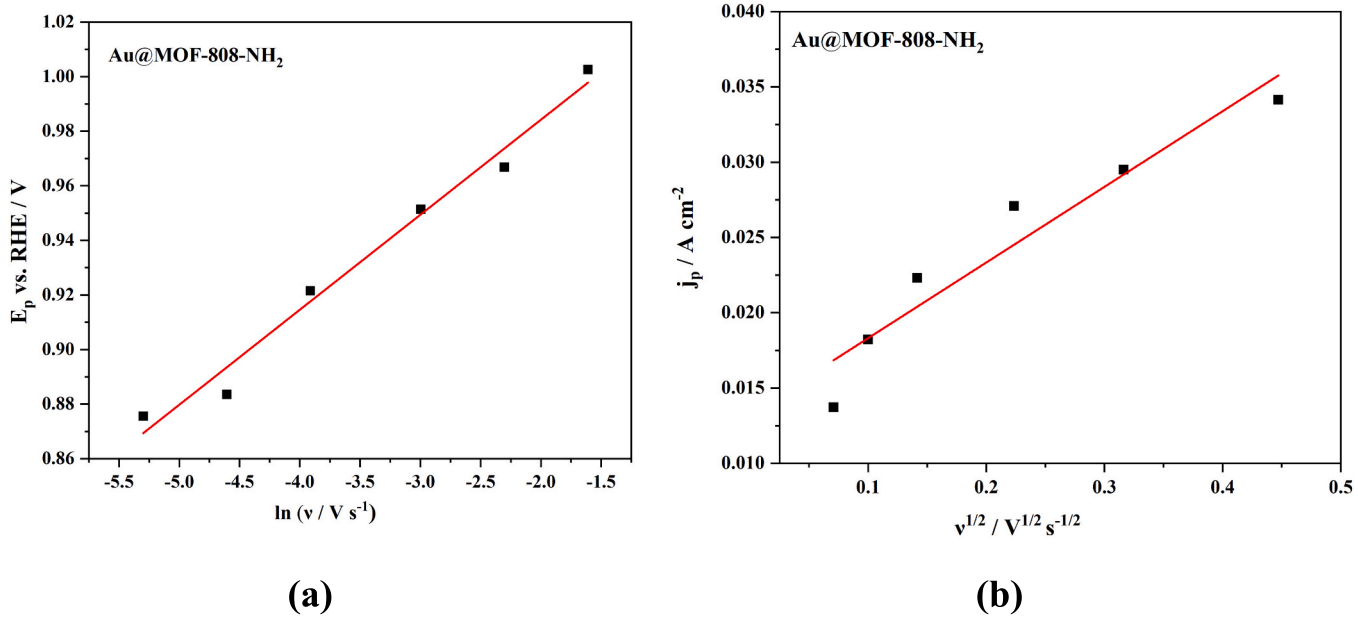

Fig. 4. (a) Plots for peak potential dependence on the logarithm of the scan rate, E_p vs. ln ν, of Au@MOF-808-NH_2 and (b) peak current as a function of the square root of the scan rate, j_p vs. $\nu^{1/2}$, of Au@MOF-808-NH_2.

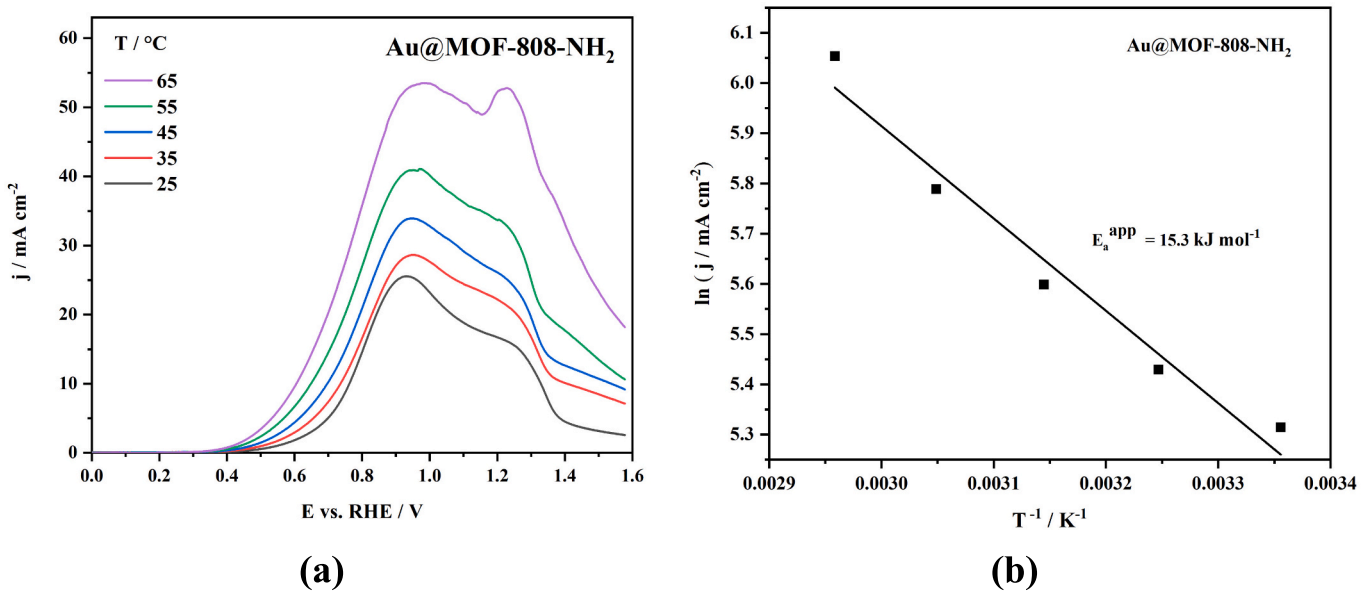

Fig. 5. (a) Effect of temperature on the LSVs of Au@MOF-808-NH_2 electrode in 0.03 M $NaBH_4$ + 2 M NaOH and (b) the corresponding Arrhenius plot.

hydrolysis reaction. For that reason, despite $NaBH_4$ solubility in water at 25 °C being around 35 wt% (55 g $NaBH_4$/100 g H_2O), most research groups have limited the $NaBH_4$ content to 20 wt% [30]. In this work, the effect of $NaBH_4$ concentration on the current density of Au@MOF-808-NH_2 was also studied. According to the Nernst equation, an increase in fuel concentration shifts the anode potential toward more negative values, thereby increasing the overall cell potential [31]. The increase in fuel concentration also enhances mass transfer and increases the overall BOR rate, further boosting current density. Fig. 6a confirms this assumption, as a steady increase in the recorded peak current densities is observed for increasing $NaBH_4$ concentration from 0.01 M to 0.12 M. The peak current density for Au@MOF-808-NH_2 observed for 0.01 M concentration amounts to 5.07 mA cm^{-2}, while the peak current density for 0.12 M concentration increases 5-fold to 24.5 mA cm^{-2}. Furthermore, as the $NaBH_4$ concentration increases, the peak potential is shifted to more positive values. This is expected for a slow electron-transfer process, typical of an irreversible process, which requires more time for complete BH_4^- depletion at the electrode surface. However, the lack of a current doubling when moving from 0.03 to 0.06 M may suggest a surface saturation effect. At low $NaBH_4$ concentrations, the BOR current increases with concentration, indicating that the reaction is at least partially limited by the availability of BH_4^- at the electrode surface. At 0.06 M, the peak current shows a minor increase, and its potential shifts significantly to more positive values, suggesting the onset of saturation effects related to surface coverage by adsorbed intermediates and/or intrinsic charge-transfer limitations at the Au@MOF-808-NH_2 active sites, which might indicate a mechanism change at higher $NaBH_4$ concentrations.

By taking the current density values for each $NaBH_4$ concentration, c_{NaBH4}, at a fixed potential, it was possible to calculate the reaction

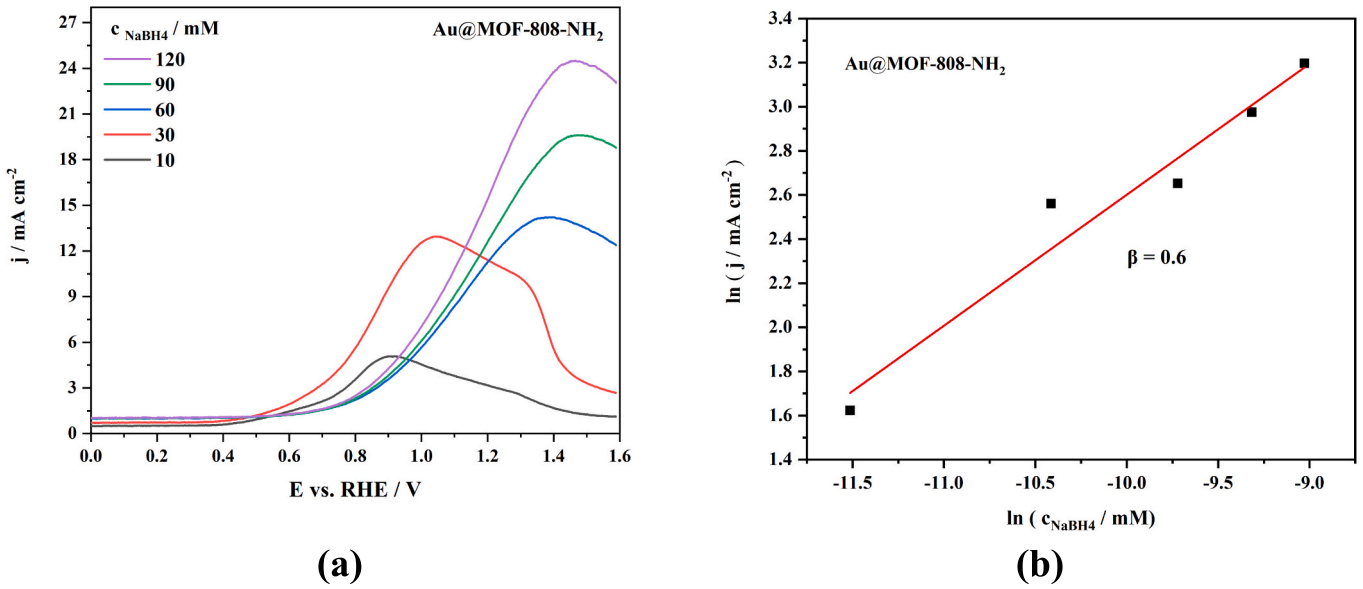

Fig. 6. (a) Effect of the $NaBH_4$ concentration in 2 M NaOH on BOR at 25 °C at 50 mV s^{-1} with the (b) corresponding ln (j) vs. ln (c_{NaBH4}) plot for Au@MOF-808-NH_2.

order, β, from the slope of the ln j vs. ln c_{NaBH4} plots, as seen in Fig. 6b. The β value for BOR at Au@MOF-808-NH_2 was determined to be 0.6, indicating that undesirable BH_4^- hydrolysis occurs in parallel with BOR, and that the electrode surface gets poisoned by adsorbed intermediates. The kinetic data were analysed and compared with the existing literature (Table 3).

The number of exchanged electrons for Au@MOF-808-NH_2 was 4.4, which is significantly higher than that reported for Ru@Fe-BTC MOF, at 1.6, but still considerably lower than for FeCo-ZNC MOF, at 7.9. Thus, compared to previously tested MOF-based BOR electrocatalysts, Au@MOF-808-NH_2 exhibits a more efficient electron-transfer process than Ru@Fe-BTC MOF but is outperformed by FeCo-ZNC MOF in this regard. The charge transfer coefficient for Au@MOF-808-NH_2, determined to be 0.63, is slightly lower than that reported for Ru@Fe-BTC MOF, which was 0.85. α is not reported for FeCo-ZNC MOF, making direct comparison inconclusive. Regarding the reaction order, the value of 0.6 for Au@MOF-808-NH_2 is lower than those for Ru@Fe-BTC MOF (0.8) and FeCo-ZNC MOF (1.0). Concerning E_a^{app}, Au@MOF-808-NH_2 exhibited the lowest value (15.3 kJ mol^{-1}), particularly compared with the other MOF-based electrocatalyst (Ru@Fe-BTC MOF, with E_a^{app} of 17 kJ mol^{-1}), suggesting a more energy-efficient electrocatalytic process.

Overall, the excellent performance of Au@MOF-808-NH_2 nanocomposite for BOR is consistent with prior reports on Au-based electrocatalysts supported on carbon materials [7,8]. While Ni- and Co-based electrocatalysts often exhibit lower onset potentials and initial activity [9,11], their susceptibility to surface oxidation and degradation under alkaline conditions can limit their long-term durability. The present results show that supporting Au NPs on MOF-808 enables high dispersion and efficient utilisation of the noble metal, achieving enhanced activity at ultralow Au loadings. This benefit is not observed in traditional carbon-supported electrocatalysts, highlighting the potential of MOF supports to reduce noble metal consumption without compromising performance. The porous structure and chemical environment of MOF-808 facilitate favourable metal–support interactions, which are expected to enhance electron transfer and improve electrocatalyst stability.

These findings complement the synergistic effects reported for bimetallic AuCo and AuNi electrocatalysts on carbon supports [10,11] and add a new dimension to electrocatalyst design based on MOF supports. Overall, MOF-supported Au electrocatalysts offer a promising pathway for developing cost-efficient anodes in DBFCs. Although the results clearly highlight the potential of Au@MOF-808-NH_2 as an effective electrocatalyst, further optimisation is necessary to enhance its performance and surpass that of currently used BOR electrocatalysts.

Table 3
Comparison of the kinetic parameters (n, α, β, and E_a^{app}) determined for Au@MOF-808-NH_2 with previously reported BOR electrocatalysts.

Electrocatalyst	n	α	β	E_a^{app} / kJ mol^{-1}	Source
Au@MOF-808-NH_2	4.4	0.63	0.6	15.3	This work
Au-Sm alloy	4.2	0.83	1.0	16.4	[32]
Au-Dy alloy	2.4	0.60	1.1	18.4	[32]
Au-Ho alloy	4.3	0.73	1.0	18.6	[32]
Au-Y alloy	4.4	0.72	1.0	20.2	[32]
AuPPy	–	–	1.0	22	[33]
Ru@Fe-BTC MOF	1.6	0.85	0.8	17	[20]
FeCo-ZNC MOF	7.9	–	1.0	–	[34]

Next, to assess this electrocatalyst's stability and potential changes in the electrochemically active surface area (ECSA) during extended BOR activity, CVs were recorded at various scan rates before and after a chronoamperometric test that simulated continuous fuel cell operation. Fig. 7a shows the CVs of Au@MOF-808-NH_2 recorded at scan rates ranging from 10 to 1000 mV s^{-1} before the CA test. The capacitive currents, represented by Δi/2, were plotted against the potential scan rate both before and after the CA test (Fig. 7b). Linear fits to these plots were used to determine the double-layer capacitance, C_{dl}, thereby allowing evaluation of changes in the ECSA resulting from modifications to the electrocatalyst surface. The ECSA is a key parameter that reflects the active surface of an electrocatalyst accessible for electrochemical reactions. A widely used non-destructive method for estimating ECSA involves measuring C_{dl} in the non-Faradaic potential region of the CV, thereby avoiding surface-altering Faradaic processes such as oxide formation or metal dissolution [35]. The C_{dl} is extracted from the slope of the linear relationship between the capacitive current density and the scan rate, as shown in Eq. 6,

$$C_{dl} = \frac{\Delta i}{2^{*}\nu} \tag{6}$$

where Δi is the difference between anodic and cathodic currents at a selected potential within the non-Faradaic region. Once C_{dl} is obtained, the ECSA can be estimated by normalising C_{dl} to the specific capacitance, C_s, of a smooth reference electrode surface, typically expressed in μF cm^{-2} (Eq. 7).

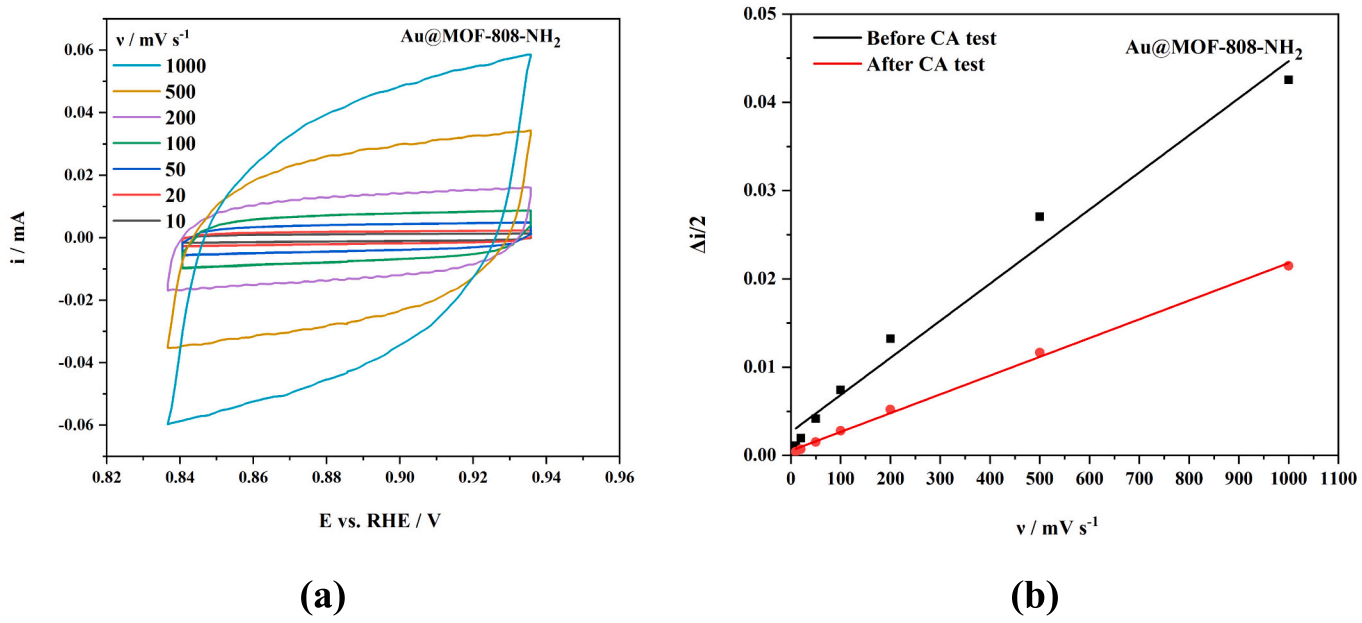

Fig. 7. (a) CVs of Au@MOF-808-NH_2 recorded in 2 M NaOH at different scan rates before the CA test. (b) Plot of the average capacitive current density, Δi/2, versus scan rate before (black) and after (red) the CA test. (For interpretation of the references to colour in this figure legend, the reader is referred to the web version of this article.)

$$\mathrm{ECSA} = \frac{C_{dl}}{C_s} \tag{7}$$

For Au electrodes in alkaline media, such as 2 M NaOH, literature values of C_s range from 20 to 40 μF cm^{-2}, with 20 μF cm^{-2} often used as a conservative estimate [35]. This method provides a practical, comparative estimate of ECSA, particularly useful for electrocatalysts with similar morphology and composition, though not as rigorous as other techniques such as underpotential deposition or oxide stripping.

After the CA test, the slope of the Δi/2 vs. ν plots (Fig. 7b), corresponding to the C_{dl}, decreased from 4.20 × 10^{-5} to 2.12 × 10^{-5} F cm^{-2}. Using Eq. 7 and a C_s of 20 μF cm^{-2}, this corresponds to an ECSA decrease from 2.10 to 1.06, when expressed as a roughness factor (dimensionless), obtained by normalising the ECSA to the geometric area of the electrode.

When multiplied by the electrode geometric area, these correspond to active surface areas of 0.147 cm^2 (before CA) and 0.074 cm^2 (after CA), indicating an area loss of ca. 50%. This reduction in ECSA evidences the susceptibility of Au@MOF-808-NH_2 to surface restructuring during prolonged operation, including NP agglomeration, partial detachment of active sites, or surface fouling. This observation aligns with the durability challenges inherent to MOF-based catalysts. While the transition from the MIL-101 family, explored in our previous work [36], to the Zr-based MOF-808-based electrocatalysts significantly improves the 'framework's resilience to alkaline media, stabilising the noble metal phase against restructuring remains a persistent hurdle.

Thus, although the results highlight the potential of MOF-based supports for BOR electrocatalysis, enhancing long-term durability remains a key challenge. Future efforts should focus on rational linker functionalisation and strengthening metal-support interactions, which can stabilise active sites and provide design principles for the next generation of DBFC anodes.

4. Conclusions

Au@MOF-808-based nanocomposite materials (Au@MOF-808, Au@MOF-808-NH_2, and Au@MOF-808-SH) were synthesised and characterised regarding their morphology, phase composition, and crystalline structure, as well as their electrocatalytic activity for the BOR was assessed.

The obtained results highlighted the critical interplay between metal NPs and MOF functionalisation in shaping the electrocatalytic performance of nanocomposite materials for BOR. Although Au NPs provide the essential electrocatalytic sites, the presence of electron-donating functional groups, particularly -NH_2, substantially enhances the accessibility and utilisation of these sites. This synergistic effect is evident in the superior activity and favourable kinetic parameters observed for Au@MOF-808-NH_2.

The high intrinsic activity and remarkably low Au loading underscore the practical advantages of these hybrid materials for real-world applications. These results open the door to designing low-cost, high-efficiency electrocatalysts by tailoring both the metal and the MOF scaffold at the molecular level.

Further research should focus on increasing the number of exchanged electrons, inhibiting BH_4^- hydrolysis, and improving the electrocatalysts' hydrophilicity to reduce bubble accumulation on the electrode surface. Additionally, it will be crucial to understand the mechanistic roles of the functional groups in stabilising reaction intermediates or modulating surface charge, as well as to scale up the synthesis for integration into practical DBFC systems.

CRediT authorship contribution statement

Ines Belhaj: Writing – original draft, Visualization, Investigation, Data curation. **J. Alexander Becker:** Writing – original draft, Investigation, Formal analysis. **Alexandre M. Viana:** Writing – original draft, Investigation. **Filipe M.B. Gusmão:** Investigation, Data curation. **Miguel Chaves:** Investigation. **Eulália Pereira:** Writing – review & editing, Conceptualization. **Biljana Šljukić:** Writing – review & editing, Supervision. **Salete S. Balula:** Writing – review & editing, Supervision, Conceptualization. **Luís Cunha-Silva:** Writing – review & editing, Supervision, Conceptualization. **Diogo M.F. Santos:** Writing – review & editing, Supervision, Conceptualization.

Declaration of competing interest

The authors declare that they have no known competing financial interests or personal relationships that could have appeared to influence

the work reported in this paper.

Acknowledgments

I. Belhaj thanks Fundação para a Ciência e a Tecnologia (FCT, Portugal) for funding a PhD grant (UI/BD/153712/2022). D.M.F. Santos thanks FCT for a Principal Researcher contract (2023.09426.CEECIND, https://doi.org/10.54499/2023.09426.CEECIND/CP2830/CT0021) in the scope of the Individual Call to Scientific Employment Stimulus - 6th Edition. The financial support of FCT under contract LA/P/0095/2020, Associated laboratory LaPMET – Laboratory of Physics for Materials and Emerging Technologies, and research unit UID/04540, CeFEMA – Centre of Physics and Engineering of Advanced Materials, is also acknowledged. This work also received financial support from the PT national funds (FCT/MECI – Ministério da Educação, Ciência e Inovação) through the project UID/50006/2025 (DOI 10.54499/UID/50006/2025) - Laboratório Associado para a Química Verde - Tecnologias e Processos Limpos. A.M. Viana thanks FCT/MCTES and ESF (European Social Fund) through POCH (Programa Operacional Capital Humano) for his PhD grant (Ref. SFRH/BD/150659/2020).

Appendix A. Supplementary data

Supplementary data to this article can be found online at https://doi.org/10.1016/j.jelechem.2026.119920.

References

[1] Ritchie, H.; Rosado, P.; Roser, M. CO_2 and Greenhouse Gas Emissions. Published online at OurWorldinData.org. 2023 Retrieved from: https://ourworldindata.org/co2-and-greenhouse-gas-emissions[Online Resource].
[2] D.M.F. Santos, Direct borohydride fuel cells (DBFCs), in: B. Šljukić, R.G. Akay, A. Bayrakçeken Yurtcan (Eds.), Direct Liquid Fuel Cells, Elsevier, 2021, pp. 203–232.
[3] L.C. Nagle, J.F. Rohan, Nanoporous gold anode catalyst for direct borohydride fuel cell, Int. J. Hydrog. Energy 36 (2011) 10319–10326.
[4] P. Manna, J. Debgupta, S. Bose, S.K. Das, A mononuclear CoII coordination complex locked in a confined space and acting as an electrochemical water-oxidation catalyst: a 'ship-in-a-bottle' approach, Angew. Chem. Int. Ed. 55 (2016) 2425–2430.
[5] B.C. Ong, S.K. Kamarudin, S. Basri, Direct liquid fuel cells: A review, Int. J. Hydrog. Energy 42 (2017) 10142–10157.
[6] A.G. Oshchepkov, G. Braesch, A. Bonnefont, E.R. Savinova, M. Chatenet, Recent advances in the understanding of nickel-based catalysts for the oxidation of hydrogen-containing fuels in alkaline media, ACS Catal. 10 (2020) 7043–7068.
[7] L. Xue, C. Liu, J. Ye, J. Zhang, L. Kang, Y. Zhang, W. Shi, W. Guo, X. Huang, X. Yang, L. Zheng, Y. Li, B. Zhang, Engineering partially oxidized gold via oleylamine modifier as a high-performance anode catalyst in a direct borohydride fuel cell, ACS Appl. Mater. Interfaces 16 (2024) 27145–27154.
[8] A. Balčiūnaitė, A. Zabielaitė, Z. Sukackienė, V. Kepenienė, D. Šimkūnaitė, A. Selskis, L. Tamašauskaitė-Tamašiūnaitė, E. Norkus, Fabrication of efficient gold–nickel-supported titania nanotube electrocatalysts for sodium borohydride–hydrogen peroxide fuel cells, Coatings 12 (2022) 850.
[9] L. Xue, W. Shi, D. Song, X. Huang, J. Zhang, Y. Zhang, W. Yuan, S. Huang, K. Sun, L. Zheng, Y. Li, C. Liu, B. Zhang, Constructing a multisite catalyst for achieving efficient and highly selective borohydride oxidation reaction, J. Colloid Interface Sci. 699 (2025) 138253.
[10] C.K. Raul, T. Chatterjee, M. Halder, R. Sinha, S. Dey, S. Basu, A.K. Meikap, Reverse micelle synthesis of Au_yNi_{100-y} nanoparticles decorated MWCNT as high-performance anode electrocatalysts for direct borohydride–hydrogen peroxide fuel cells, ChemNanoMat 11 (2025) e202500005.
[11] C.K. Raul, S. Dey, M. Halder, R. Karmakar, S. Basu, A.K. Meikap, Synthesis of Au_xCo_{100-x}/MWCNT nanoparticles as an efficient anode electrocatalyst for borohydride oxidation in alkaline medium, J. Appl. Electrochem. 53 (2023) 977–990.
[12] L. Yi, W. Wei, C. Zhao, L. Tian, J. Liu, X. Wang, Enhanced activity of au–Fe/C anodic electrocatalyst for direct borohydride–hydrogen peroxide fuel cell, J. Power Sources 285 (2015) 325–333.
[13] D. Duan, J. Feng, X. You, X. Zhou, Y. Wang, L. Chen, S. Liu, Evaluation of co–au bimetallic nanoparticles as anode electrocatalyst for direct borohydride-hydrogen peroxide fuel cell, Ionics 27 (2021) 5157–5166.
[14] S.C. Fernandes, A.M. Viana, B. de Castro, L. Cunha-Silva, S.S. Balula, Synergistic combination of the nanoporous system of MOF-808 with a polyoxomolybdate to design an effective catalyst: simultaneous oxidative desulfurization and denitrogenation processes, Sustain. Energy Fuels 5 (2021) 4032–4040.
[15] F. Mirante, P. Leo, C.N. Dias, L. Cunha-Silva, S.S. Balula, MOF-808 as an efficient catalyst for valorization of biodiesel waste production: glycerol acetalization, Materials 16 (2023) 7023.
[16] K. Rezapour, B. Habibi, H. Imanzadeh, New type nanocomposite based on metal-organic frameworks decorated with nickel nanoparticles as a potent electrocatalyst for methanol oxidation in alkaline media, Int. J. Hydrog. Energy 69 (2024) 518–531.
[17] B. Habibi, A. Pashazadeh, S. Pashazadeh, L.A. Saghatforoush, A new method for the preparation of MgAl layered double hydroxide–copper metal–organic frameworks structures: application to electrocatalytic oxidation of formaldehyde, Nature 14 (2024) 5222.
[18] K. Rezapour, B. Habibi, H. Imanzadeh, Bio-MOF/nano carbon black composite on the carbon felt as an electrocatalyst for oxidation of urea, Int. J. Hydrog. Energy 184 (2025) 151857.
[19] B. Habibi, A. Pashazadeh, S. Pashazadeh, Electrosynthesis/chemical in situ growth of the LDH/MOFs nanocomposite at the surface of carbon ceramic electrode for methanol oxidation reaction, Ionics 31 (2025) 8245–8261.
[20] G. Backović, B. Šljukić, G.S. Kanberoglu, M. Yurderi, A. Bulut, M. Zahmakiran, D. M.F. Santos, Ruthenium(0) nanoparticles stabilized by metal–organic framework as an efficient electrocatalyst for borohydride oxidation reaction, Int. J. Hydrog. Energy 45 (2020) 27056–27066.
[21] N. Sun, S.S.A. Shah, Z. Lin, Y.-Z. Zheng, L. Jiao, H.-L. Jiang, MOF-based electrocatalysts: an overview from the perspective of structural design, Chem. Rev. 125 (2025) 2703–2792.
[22] G. Gupta, F. Gusmão, A. Paul, B. Šljukić, D.M.F. Santos, J. Lee, M. Guedes da Silva, A. Pombeiro, C. Lee, A mixed-ligand co metal–organic framework and its carbon composites as excellent electrocatalysts for the oxygen evolution reaction in green-energy devices, Dalton Trans. 53 (2024) 5001–5009.
[23] H. Wang, X. Liu, W. Yang, G. Mao, Z. Meng, Z. Wu, H.-L. Jiang, Surface-clean Au_{25} nanoclusters in modulated microenvironment enabled by metal–organic frameworks for enhanced catalysis, J. Am. Chem. Soc. 144 (2022) 22008–22017.
[24] A. Oshchepkov, G. Braesch, G. Rostamikia, A. Bonnefont, M. Janik, M. Chatenet, E. Savinova, Insights into the borohydride electrooxidation reaction on metallic nickel from operando FTIRS, On-Line DEMS and DFT, Electrochim. Acta 389 (2021) 138721.
[25] D.M.F. Santos, C.A.C. Sequeira, Determination of kinetic and diffusional parameters for sodium borohydride oxidation on gold electrodes, J. Electrochem. Soc. 156 (2009) F67–F72.
[26] C. Celik, F.G. Boyaci San, H.I. Sarac, Effects of operation conditions on direct borohydride fuel cell performance, J. Power Sources 185 (2008) 197–201.
[27] J. Ma, Y. Sahai, R.G. Buchheit, Direct borohydride fuel cell using Ni-based composite anodes, J. Power Sources 195 (2010) 4709–4713.
[28] A.J. Bard, L.R. Faulkner, Electrochemical Methods: Fundamentals and Applications, 2nd ed., Wiley, New York, 2001.
[29] M.T.M. Koper, Thermodynamic theory of multi-electron transfer reactions: implications for electrocatalysis, J. Electroanal. Chem. 660 (2011) 254–260.
[30] T.H. Lee, S.S. Yu, T.H. Oh, Effect of anode conditions on the performance of direct borohydride–hydrogen peroxide fuel cell system, Int. J. Hydrog. Energy 48 (2023) 18845–18855.
[31] M.G. Hosseini, N. Rashidi, R. Mahmoodi, M. Omer, Preparation of Pt/G and PtNi/G nanocatalysts with high electrocatalytic activity for borohydride oxidation and investigation of different operation condition on the performance of direct borohydride–hydrogen peroxide fuel cell, Mater. Chem. Phys. 208 (2018) 207–219.
[32] G. Backović, J. Milikić, S. De Negri, A. Saccone, B. Šljukić, D.M.F. Santos, Enhanced borohydride oxidation kinetics at gold–rare earth alloys, J. Alloys Compd. 857 (2021) 158273.
[33] J. Milikić, A. Tapia, U. Stamenović, V. Vodnik, M. Otoničar, S. Škapin, D.M. F. Santos, B. Šljukić, High-performance metal (au, cu)–polypyrrole nanocomposites for electrochemical borohydride oxidation in fuel cell applications, Int. J. Hydrog. Energy 47 (2022) 36990–37001.
[34] S. Kottarathil, S. Narayanaru, S. Unni, T. Tamaki, H. Kuroki, U. Hareesh, G. Anilkumar, T. Yamaguchi, Selective borohydride oxidation reactions of zeolitic imidazolate framework-derived bimetallic carbon alloy electrocatalysts for alkaline fuel cell applications, ACS Appl. Energy Mater. 5 (2022) 12571–12582.
[35] C.M. Schott, P.M. Schneider, K.-T. Song, H. Yu, R. Götz, F. Haimerl, E. Gubanova, J. Zhou, T.O. Schmidt, Q. Zhang, V. Alexandrov, A.S. Bandarenka, How to assess and predict electrical double layer properties: implications for electrocatalysis, Chem. Rev. 124 (2024) 12391–12462.
[36] I. Belhaj, A. Becker, A.M. Viana, F.M.B. Gusmão, M. Chaves, B. Šljukić, S.S. Balula, L. Cunha-Silva, D.M.F. Santos, Au–MIL nanocomposites with enhanced borohydride oxidation kinetics for potential use in Direct liquid fuel cells, Energies 18 (2025) 4503.